Supporting Information

Parallel *p-n* Junctions across Nanowires by One-Step *ex-situ* Doping

Ori Hazut[1], Bo-Chao Huang[2], Adi Pantzer[3], Iddo Amit[4], Yossi Rosenwaks[4], Amit Kohn[3], Chia-Seng Chang[5], Ya-Ping Chiu[2], and Roie Yerushalmi[1*]*

[1] Institute of Chemistry and the Center for Nanoscience and Nanotechnology, The Hebrew University of Jerusalem, Edmond J. Safra Campus, Givat Ram, Jerusalem, 91904, Israel.

[2] Department of Physics, National Sun Yat-sen University, Kaohsiung, 80424, Taiwan.

[3] Department of Materials Engineering and the Ilse Katz Institute for Nanoscale Science and Technology, Ben-Gurion University of the Negev, Beer-Sheva 8410501, Israel.

[4] Department of Physical Electronics, School of Electrical Engineering, Tel-Aviv University, Tel-Aviv 69978, Israel.

[5] Institute of Physics, Academia Sinica, Nankang, Taipei 115, Taiwan.

Diffusion and electrical simulation

The Sentaurus TCAD by Synopsys Inc. was used to model dopant diffusion and calculate the NW junction electrical properties. The 2D diffusion of P and B into the Si NW structure was modeled by the Sentaurus process simulator. The contact doping process was modeled by constructing a model and simulating the diffusion process. The model was constructed by placing an oxide layer with a constant dopant concentration (C_{Surf}^{CD}) in contact with the NW surface. The proximity doping process was modeled by the evaporation of an oxide layer with a constant doping concentration (C_{Surf}^{PD}) onto the NW circumference facing the respective donor substrate. The simulated evaporation process accounts for the variation in dopant projection flux onto the NW surface. The initial dopant distributions described above for the CD and PD processes were then used as initial conditions for the diffusion simulation. The simulation employed the five-stream diffusion model[1,2] to simulate the coupled diffusion of dopants and defects. Three separate differential equations were solved for dopant atoms flux, two equations were solved for vacancy and interstitial defects, and two equations were solved for dopant-vacancy and dopant-interstitial pairs. The simulation also accounted for the segregation of dopants at the Si−Si dioxide interface and the clustering of dopants and defects.[3-5]

Figure S1 presents the initial dopant concentrations and the resulting dopant distribution before and after the diffusion process simulations. In addition, the simulated and experimental temperature profiles are presented. Combinations of both contact and proximity doping processes were modeled, and a best-fit analysis for the simulated dopant distributions and measured dopant distributions, extracted from the XSTM results, was performed by varying the initial dopant concentrations for the contact and proximity doping simulations (C_{Surf}^{CD} and C_{Surf}^{PD}, respectively). The relative contributions of each process were calculated from the best-fit dopant distribution.

The best-fit dopant distribution was used to calculate NW junction electronic properties using the Sentaurus device simulator.

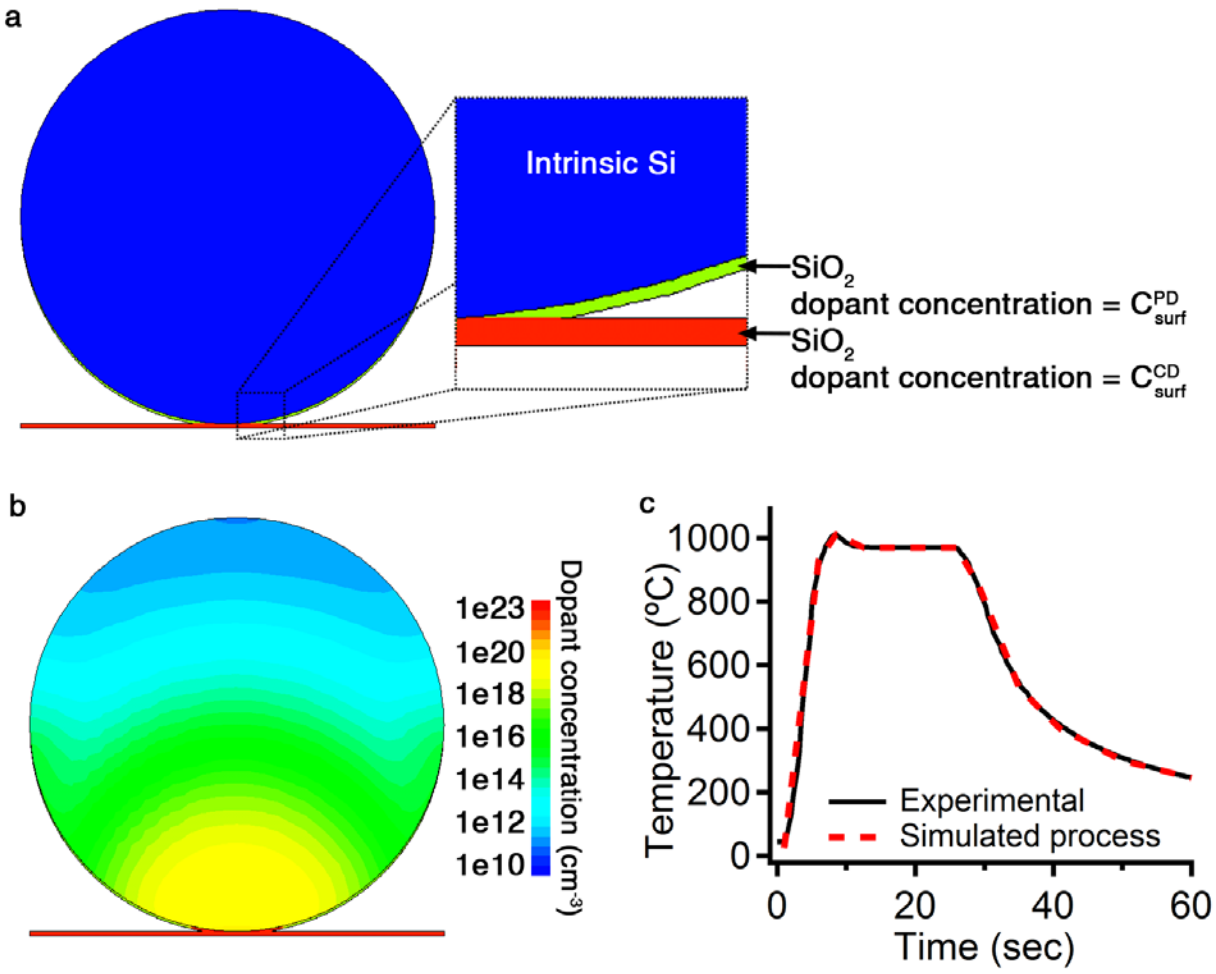

Figure S1. NW model structure used for the simulations. (a) Initial dopant distribution prior to the diffusion simulation step and (b) dopant distribution after the diffusion simulation. (c) Experimental and simulated temperature profiles used for the dopant diffusion process simulation.

XSTM measurements

1. Cleavage process and XSTM measurements

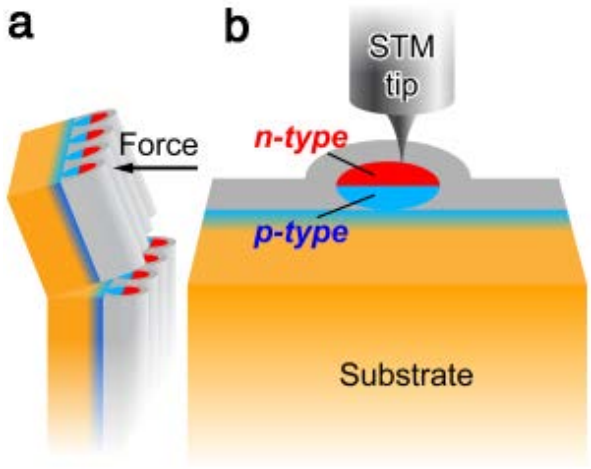

Figure S2. (a) Schematic of the sample cleavage procedure in the XSTM measurements. (b) Schematic depiction of the XSTM measurements.

A substrate with *p*-*n*-doped Si NWs was patterned with an aluminum grid (100 nm thick) on top of the Si NWs by a standard photolithography and lift-off process. The sample was cleaved *in situ* in the STM chamber at UHV at room temperature to obtain a cross-sectional slice of the NW (Figure S2). All STM experiments reported here were performed in an UHV chamber with a base pressure of approximately 5×10^{-11} Torr.

2. Geometrical structure of the cleaved p-n doped Si NW

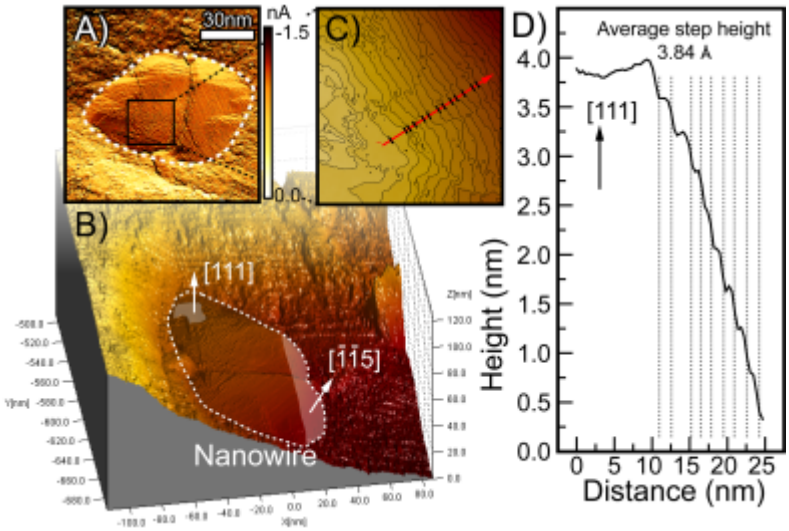

Figure S3. (A) Cross-sectional STM image of a parallel *p*-*n*-doped Si NW. (B) Three-dimensional STM image. The white dotted curves indicate the outline of the cleaved NW. (C) Atomic-scale height contour across the NW. A transverse line is indicated by the red arrow in (C), and the corresponding height profile of the NW is shown in (D) with an average step height of 3.84 Å across the Si NW along the [111] direction.

3. Electronic dI/dV images of the Si NW

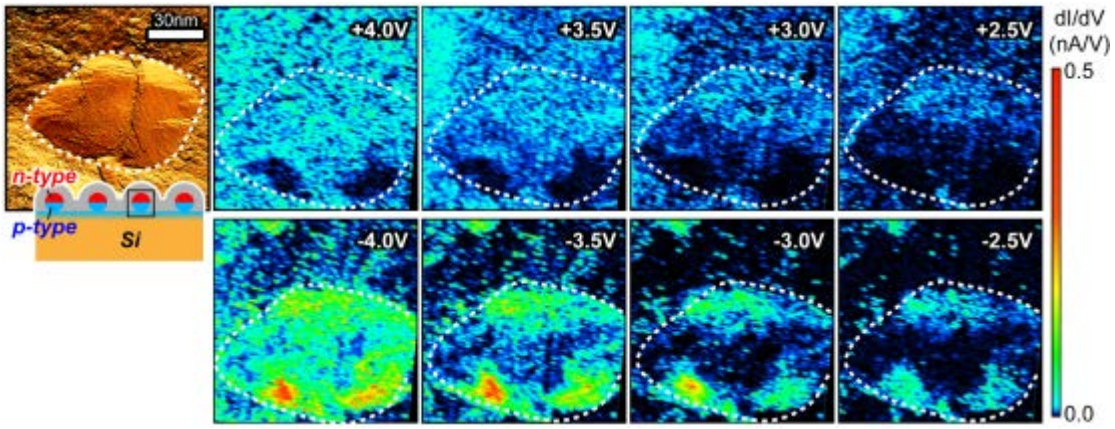

Figure S4. XSTM topography image of the NW and corresponding spectroscopic *dI/dV* information for the NW recorded for a sample bias of +4.0 V to -4.0 V. The white dotted curves indicate the outline of the cleaved NW.

4. Band structure of the cleaved p-n doped Si NW

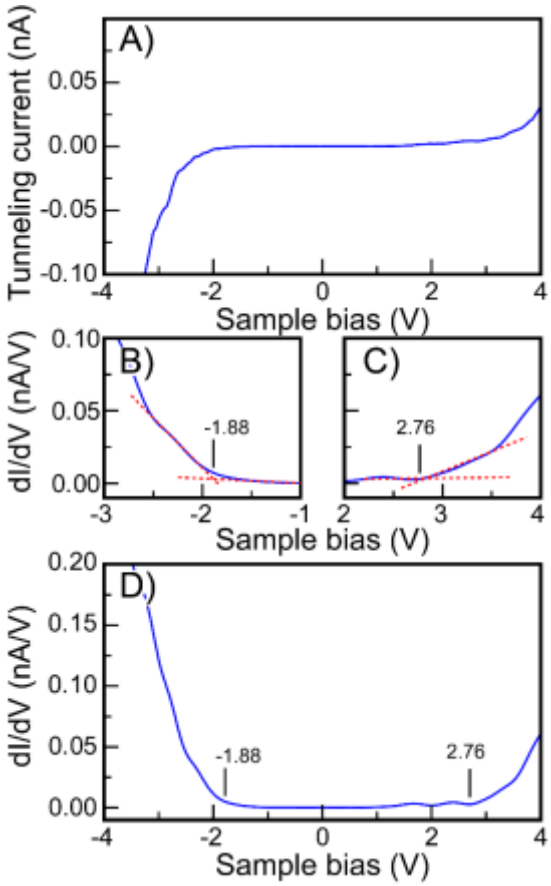

Figure S5. Determination of the band edge positions for the *p*-*n*-doped Si NW. (A) Tunneling current obtained at different bias voltages. The approximate locations of the valence-band maximum (E_v) and conduction-band minimum (E_c) were determined by assuming linear onsets in the differential conductance (dI/dV) in (B) and (C), respectively.[6-8] (D) The band edge onset position and band-gap size were determined.

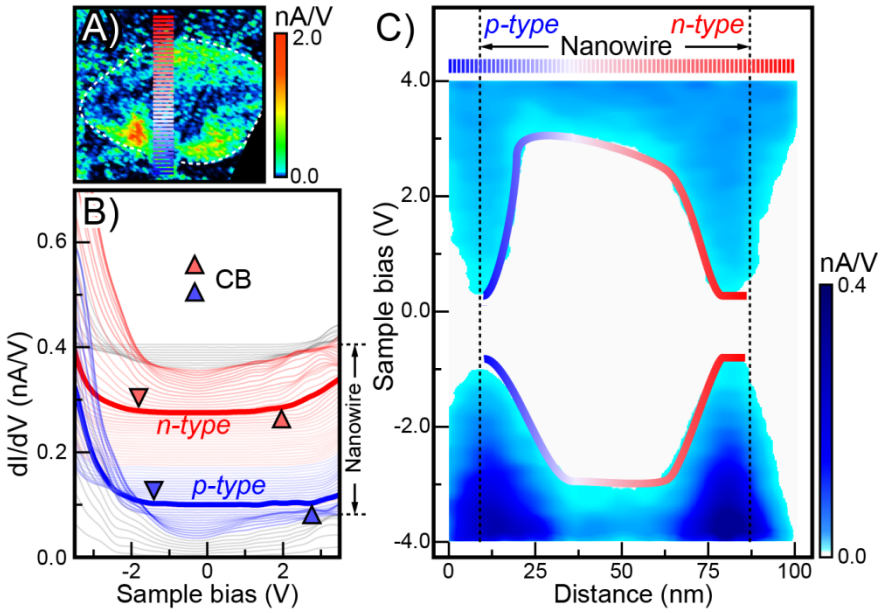

Figure S6. Band structure of the *p*-*n*-doped Si NW. (A) Spectroscopic *dI/dV* (-3.5 V) data of a parallel *p*-*n*-doped Si NW recorded at a sample bias of -3.5 V. (B) Point-to-point *dI/dV* curves with 1.2 nm resolution were measured for the *p*-type region (blue curves) across the NW to the *n*-type region (red curves). The corresponding positions are indicated by color bars in (A). The electronic spectra across the *p*- and *n*-doped regions can be distinguished. In the scanning tunneling spectroscopy measurements, the zero sample bias is indicated by the energetic position of the Fermi level. The presence of B-doped (P-doped) Si exhibits a *p*-type (*n*-type) electronic character, which is detected where the conduction band (CB) edge is far from (close to) the Fermi level. (C) Band alignment mapping across the *p*-*n* Si NW based on the characteristics of the spatial spectroscopic measurements in (B).

5. Theoretical analysis of spectroscopic data

[A] Tip-induced band bending (TIBB) effects during STM measurements

Scanning-tunneling microscopy (STM) and scanning tunneling spectroscopy (STS) measurements have been well recognized as an ideal technique to study local electronic states within a few electron volts of the Fermi level. In the case of STS of semiconductor surfaces, because an extended region of space charge can exist at the surface of a semiconductor, the measurements would cause some of the applied potential between the tip and sample being dropped in the semiconductor itself. The general schematic band structure relating the electric field at the surface of a semiconductor to the electrostatic potential difference across the semiconductor space charge region is shown in Figure S7. In addition, the effect of the applied potential extending into the semiconductor rigidly shifts the band edges and thus reduces the value of tunneling current from the tip to the sample. This effect is termed the "tip-induced band bending" (TIBB) effect.[9,10]

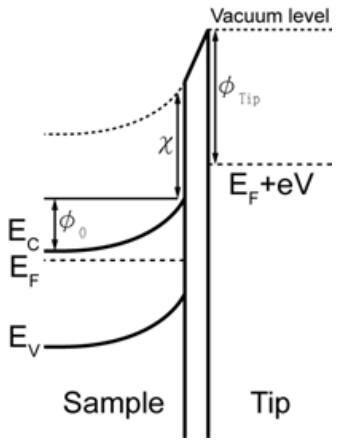

Figure S7. Schematic band structure of a metallic tip approaching a semiconducting sample. The valence-band maximum EV and conduction-band minimum EC indicate the band edge positions of the sample, where V is the applied voltage on the tip, EF is the sample Fermi level, and EF+eV is the tip Fermi level. The band bending at the surface is denoted by φ0. E-EF=eV-φ0, where φ0 is the TIBB effect on the surface.

[B] Three-dimensional (3D) potential computation technique for estimating the TIBB effect

The electrostatic effects introduced by a voltage-biased tip near a semiconductor were considered. The analysis method was based on the 3D potential computation technique for estimating the TIBB effect.[6,11] To solve the 3D electrostatic problem of a metallic probe tip close to the surface of a semiconductor, in the calculation code, a prolate spheroidal coordinate system was adopted for the vacuum and a Cartesian coordinate system was utilized for the semiconductor, as illustrated in Figure S8. The computer program implementation received input parameters, such as the tip-sample separation (d), opening angle (θ) of the tip, and radius of curvature of the tip (R), that were appropriately specified for the physical conditions present during the experiments.

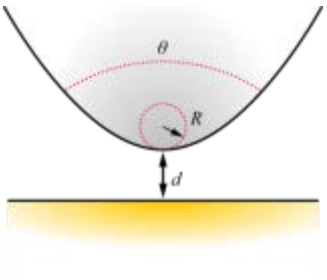

Figure S8. Illustration of the spheroidal coordinates. The probe tip is specified by the radius of curvature R and opening angle θ. The sample-tip distance is d.

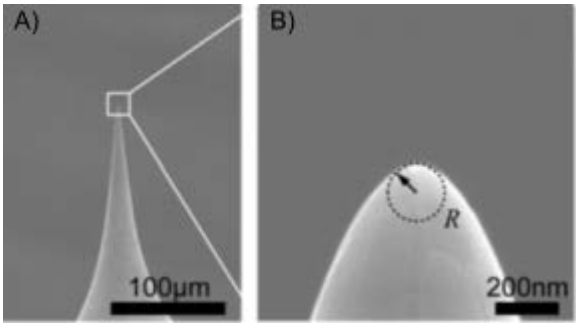

Figure S9. SEM image of a probe tip used to extract the required parameters. (A) Low- and (B) high-magnification images. An R value of 90 nm and θ of 124° were obtained.

[C] Extraction of the dopant concentrations from the spectroscopic data

Representative simulated tunneling spectra of the *n*-doped Si surface, obtained using the 3D electrostatic computation model, are shown in Figure S10. Good agreement between the simulated and measured tunneling spectra of the *n*-doped Si surface was achieved for a tip-sample distance (*d*) of 0.7 nm and a dopant concentration of 10^{19} cm^{-3}. A tip radius of curvature (*R*) value of 90 nm, a work function of the W tip of 4.5, and an electron affinity of Si of 4.05 eV were used as the input parameters in our calculations.

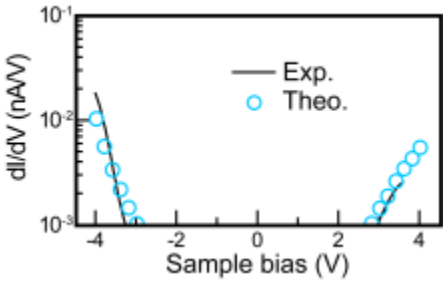

Figure S10. Comparison of the tunneling spectra of the Si surface between the experiments (black curve) and simulations (blue circles).

[D] Extraction of the surface potential from the spectroscopic data

The impact of the TIBB effect can be estimated numerically using the 3D potential computational model. The variation of the surface potential as a function of the sample bias when STM measurement was performed on the *n*-doped Si surface is presented in Figure S11.

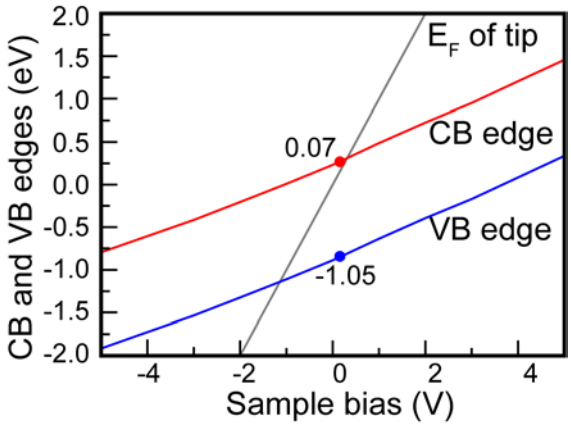

Figure S11. Sample surface potential. The red and blue curves indicate the CB and VB edges, respectively, under the TIBB effect. The gray line indicates the Fermi level of the tip.

From the theoretical model shown in Figure S11, the energetic positions of the CB and VB edges of *n*-doped Si surface (dopant concentration of 10^{19} cm^{-3}) without the applied sample bias (at the zero sample bias) were estimated to be +0.07 and -1.05 V, respectively.

Additionally, when we accounted for the band bending effect in the semiconductor, we were able to numerically derive the electrostatic potential as a function of distance to the semiconductor and the transmission through the space-charge region. Figure S12 representatively depicts the electrostatic potential as a function of distance at the zero sample bias when STM measurements are performed on the Si surface. A more quantitative understanding of our STM experimental results can be found in the literature.[6,12-17]

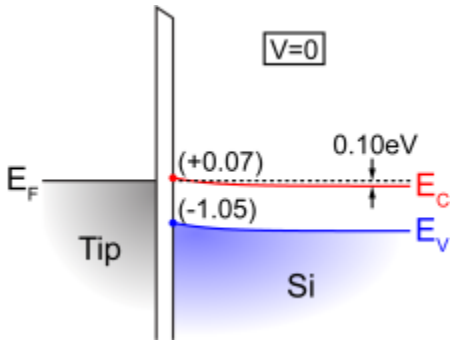

Figure S12. Theoretical calculations for the band edges of the *n*-doped Si surface.

Off-axis electron holography

Sample preparation

Cross-sectional TEM samples of several doped and intrinsic NW were prepared by an FEI Strata Dual Beam FIB using Ga ions at energies of 30 and 5 keV. The regions of interest on the Si wafer surfaces were protected from normal incidence Ga ions by the sputtering of a thin layer of SiO_2 (TEOS, approximately 100 nm thick) and the deposition of a thick layer of platinum (Pt).

Three main requirements were addressed for the OAEH experiments when preparing the TEM samples by FIB: 1) uniform sample thickness; 2) the region of interest was located at the sample edge to form the interference pattern of the hologram; and 3) sample preparation was completed with low-energy ion milling to reduce sample damage (negligible electrically inactive crystalline regions and 10 nm of amorphization[18]).

To obtain a uniform sample thickness, the sample lamella was lifted out and milled from the back side, the substrate side,[19] as shown in Figure S13. The sample was electrically grounded to the grid holder by depositing Pt to reduce the influence of the electron beam on the concentration of charge carriers.[20]

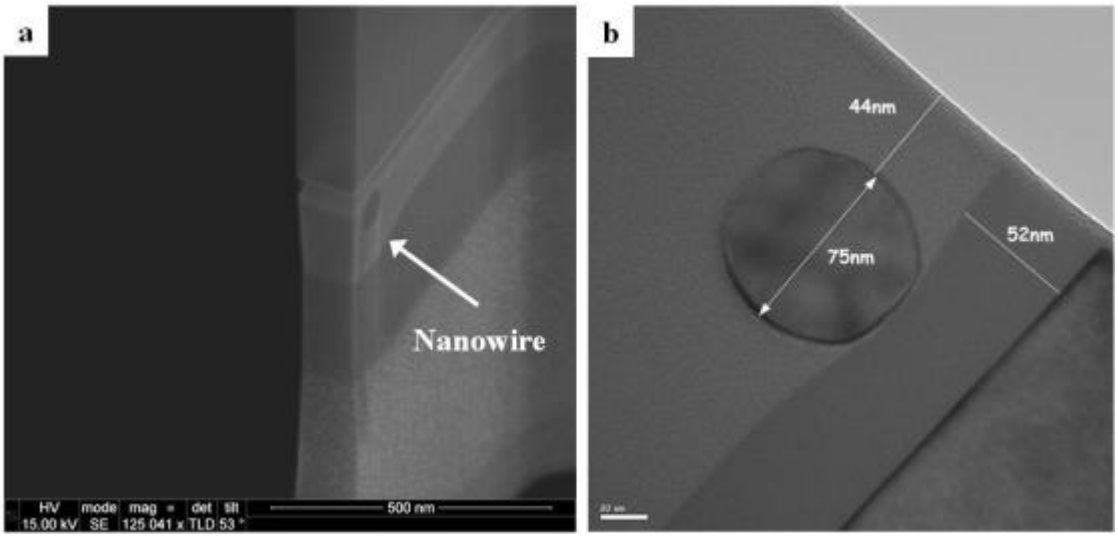

Figure S13. (a) SEM secondary electron side-view images of a FIB-prepared sample displaying uniform thickness, which is suitable for examination by off-axis electron holography. (b) Bright-field TEM image of the intrinsic NW sample showing the Si NW (75 nm in diameter) located 44 nm from the edge of the TEM sample. The NW was encapsulated in SiO_2, TEOS from the top, and thermally oxidized Si (52 nm thick) from the bottom.

Measurements

Mapping of the sample thickness by EFTEM

The sample thickness was mapped by energy-filtered TEM (EFTEM) to verify uniform thickness (Figure S14) using a Tridiem Gatan Image Filter (GIF), operated with a convergence angle of under 1 mrad and a collection angle of 18.5 mrad. An example measurement, shown in Figure S14, demonstrates the uniform and appropriate thickness of the sample. The inelastic mean free path of electrons in Si was measured for the optical conditions in these measurements at 153±2 nm. The inelastic mean free path was determined with high accuracy using a recently

developed method of additional cross-sectioning by FIB of the TEM sample, as described in ref. *18*.

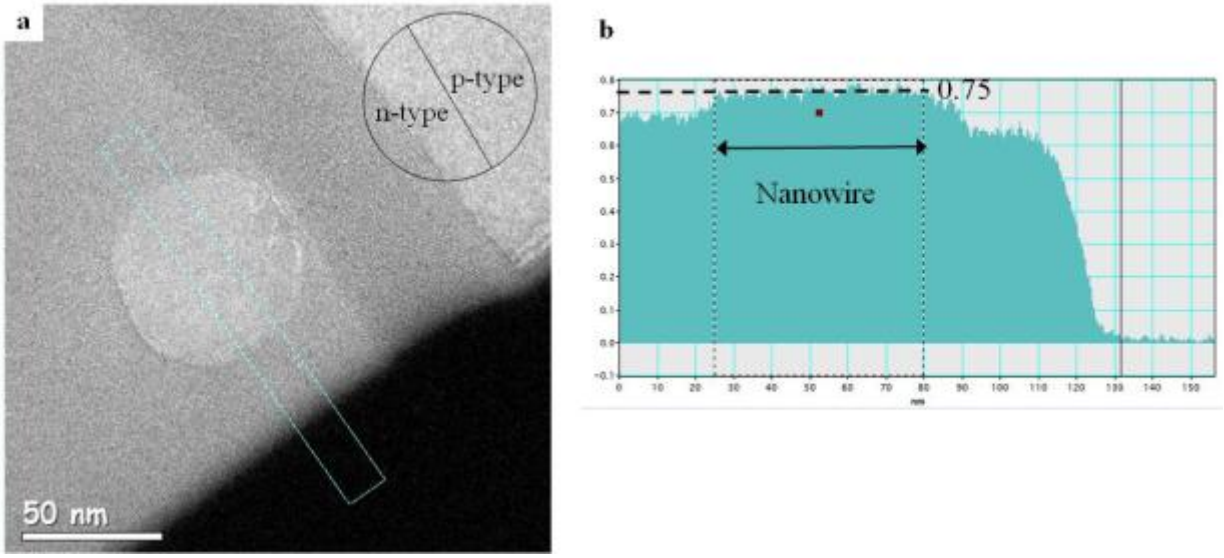

Figure S14. (a) Thickness map of doped NW calculated from energy-filtered TEM images. (b) Thickness of the sample along the direction denoted schematically by the blue rectangle in (a) in units of inelastic mean free path.

OAEH experiment

OAEH experiments were undertaken using an adapted JEOL JEM 2100F for Lorentz microscopy[21] operated at an accelerating voltage of 200 kV and characterized by a point resolution of 2 nm. The holograms were recorded using a 2,048x2,048-pixel Gatan Ultrascan charge coupled device (CCD) camera, as shown in Figure S15. All samples were tilted slightly away from the Si<011> zone axis orientation to reduce diffraction contrast or bend contours.

The typical biprism voltage for recording holograms was 90 V, and a nominal magnification of x40,000 at the CCD camera resulted in a 0.25 nm pixel size for the hologram. The contrast levels of the holograms for the sample and vacuum were approximately 25% and 40%, respectively,

with an average intensity of approximately 300 counts. Phase reconstruction was performed using between 100 and 128 pixels on the side band without removing the streak related to the Fresnel contrast of the biprism, resulting in approximately 4-5 nm per pixel in the reconstructed phase images. A reference hologram from the vacuum was used for phase reconstruction.

The hologram and reference vacuum hologram were collected using the Holoworks5 plug-in for the Gatan Digital Micrograph software. The phase and amplitude were reconstructed from the holograms using scripts provided by Arizona State University (*e.g.*, ref. *22*) within the Gatan Digital Micrograph software. The reconstructed phase was flattened according to the vacuum region near the sample region and translated into variations in the electrostatic potential assuming constant thickness of the entire sample and mean inner potential along the electron trajectory.

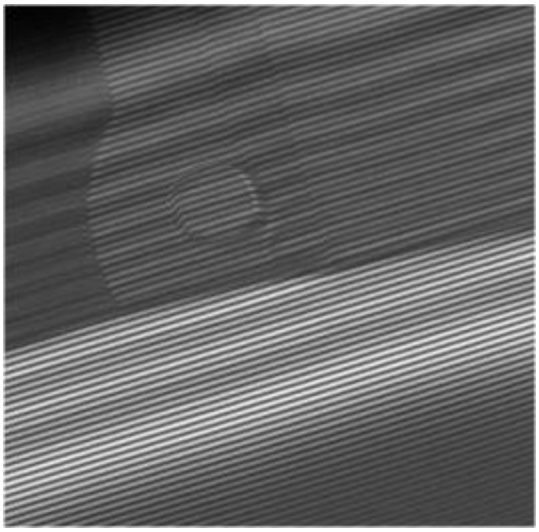

Figure S15. Example of an electron hologram collected for an intrinsic NW sample

Comparison of built-in potential measurements between doped and intrinsic NWs

Variations in the electrostatic potential were measured for doped and intrinsic NWs. Due to the spatial resolution of this methodology compared with the diameter of the NW, the aims of these measurements were as follows:

I. Verify a parallel p-n junction in the NWs by mapping the mean inner potential (MIP) in a cross-sectional view.

II. Measure the built-in potential within the accuracy of this methodology, which is approximately 0.2 V.

Figures S16 and S17 present variations in the electrostatic potential across the NWs and in the surrounding material for intrinsic and doped NWs, respectively. The line scans indicate the potential variations perpendicular and parallel to the *p*-*n* junction, which correspond in the figure from left to right and top to bottom, respectively. For the intrinsic NW, the variations in the potential in both directions were approximately 0.2 V, which is within the sensitivity of this technique. Therefore, the band structure in the intrinsic NW is flat within the 0.2 V sensitivity of this method. Significant differences in the variation of the potential in the two directions were observed for the doped NW. Parallel to the junction, the potential variations were again within 0.2 V. However, a significant variation in the electrostatic potential was measured perpendicular to the PN junction, corresponding to a built-in potential of approximately 1 V.

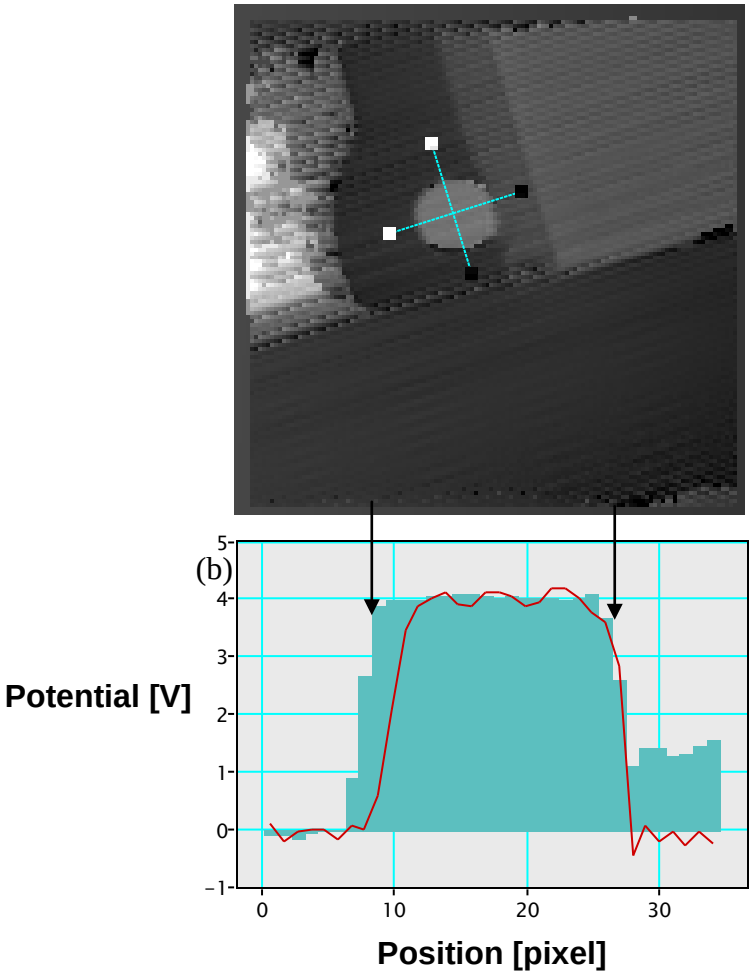

Figure S16. (a) Calculated map of the variations of the electrostatic potential in an intrinsic Si NW with a diameter of 75 nm (sample is 177 nm thick). Each pixel is 5.1 nm in lateral distance. (b) Line scans of the variations in the electrostatic potential values along the directions represented schematically by the lines in (a). The green line represents the variations in the electrostatic potential along the horizontal direction; the red line represents the variations in the electrostatic potential along the vertical direction. Arrows indicate the onset of the NW, as determined from bright-field TEM images.

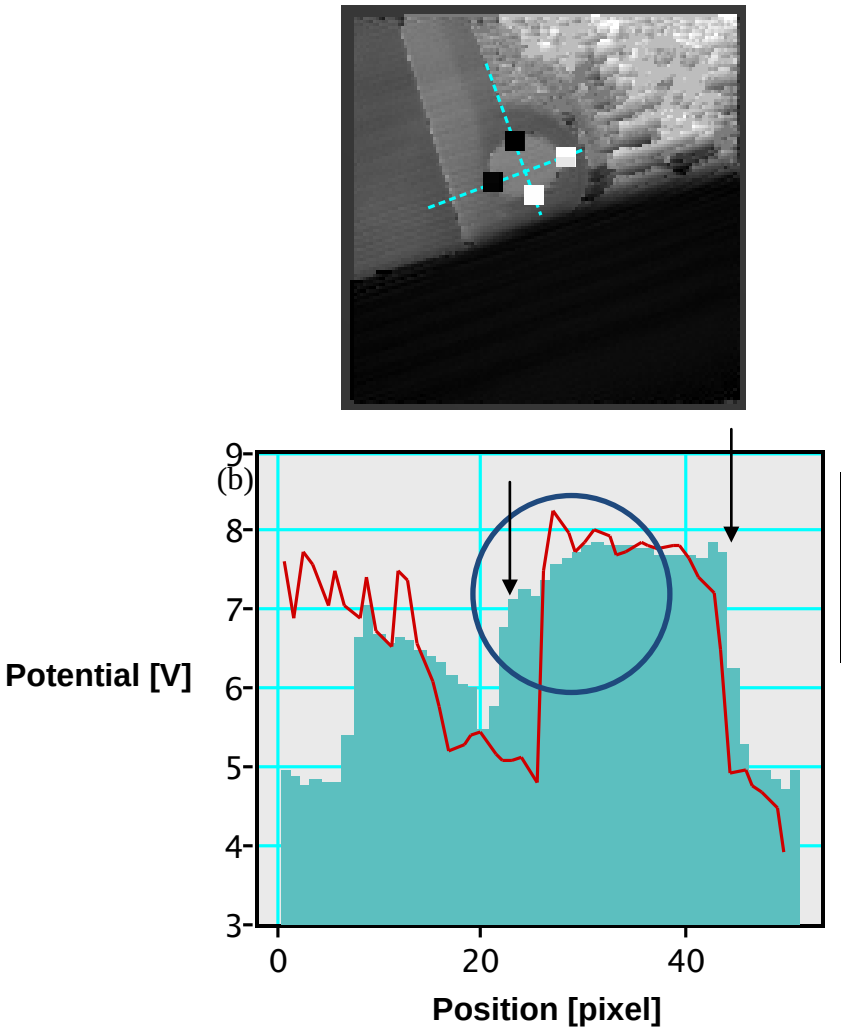

Figure S17. (a) Calculated map of the variations in the electrostatic potential of a doped Si NW with a diameter of 83 nm (sample is 195 nm thick). Each pixel is 5.1 nm in lateral distance. (b) Line scans of the variations in the electrostatic potential along the directions represented schematically by the lines in (a). The green line represents the variations in the electrostatic potential along the horizontal direction (perpendicular to the *p-n* junction); the red line represents the variations in the electrostatic potential values from along the vertical direction (parallel to the *p-n* junction). Arrows indicate the onset of the NW, as determined from bright-field TEM images, and the blue circle highlights potential variations due to the band structure.

The electrostatic potential measurements as a function of position within the NW, perpendicular to the junction, for a doped NW and intrinsic NW are presented in Figure S18. The position of the edge of the NW was determined by comparing bright-field TEM images and the reconstructed phase maps.

The electrostatic potential variation measurements for doped NWs across the interface between the *n*- and *p*-type regions also exhibited a built-in potential of 1.0±0.2 V, which is in agreement with the expected variation based on the doping levels.

The electrostatic potential variation measurements for the intrinsic NW across the interface suggested an approximately constant electrostatic potential throughout the NW, within the 0.2 V accuracy of this method.

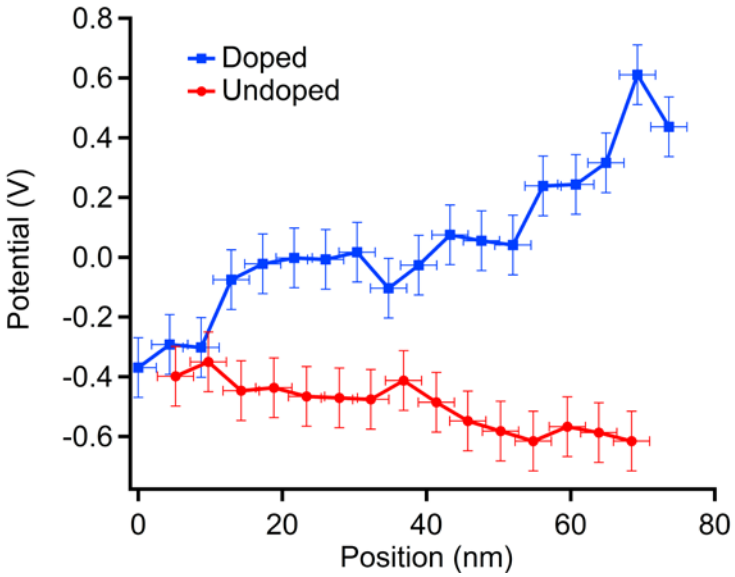

Figure S18. Comparison of the variations of the electrostatic potential perpendicular to the pn junction of a doped NW and compared to a similar line profile across an intrinsic NW.

A final demonstration of the potential variations in doped and intrinsic NWs was performed by quantitative mapping of the electrostatic potential variations within the NWs. Potential mapping was performed for intrinsic (Figure S19) and doped (Figure S20) NWs. Mapping of an intrinsic NW suggested an approximately constant electrostatic potential throughout the NW, within the 0.2 V accuracy of the OAEH method, whereas the formation of a p-n junction was observed in the doped NW.

Fresnel contrast bands can be observed in these maps due to the biprism.

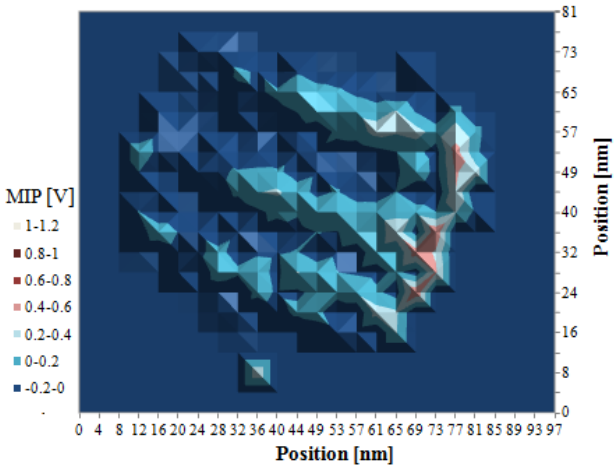

Figure S19. Map of the variations of the electrostatic potential in a cross-sectional view of an intrinsic NW. The color code denotes the values of the potential variations.

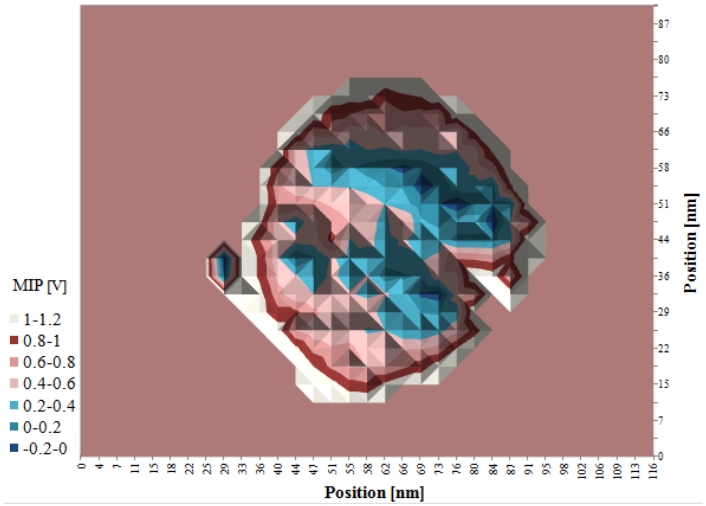

Figure S20. Map of the variations of the electrostatic potential in a cross-sectional view of a doped NW. The color code denotes the values of the potential variations.

REFERENCES

1. Dunham, S. T.; Gencer, A. H.; Chakravarathi, S. Modeling of Dopant Diffusion in Silicon. *IEICE Trans. Electron.* **1999**, E82C, 800-812.

2. Dunham, S. T. A Quantitative Model for the Coupled Diffusion of Phosphorus and Point-Defects in Silicon. *J. Electrochem. Soc.* **1992**, 139, 2628-2636.

3. Lau, F.; Mader, L.; Mazure, C.; Werner, C.; Orlowski, M. A Model For Phosphorus Segregation at the Silicon Silicon Dioxide Interface. *Appl. Phys. A Mater. Sci. Process.* **1989**, 49, 671-675.

4. Zographos, N.; Zechner, C.; Avci, I. Efficient TCAD Model for the Evolution of Interstitial Clusters, {311} Defects, and Dislocation Loops in Silicon. *Mater. Res. Soc. Online Proc. Libr.* **2007**, 994.

5. Law, M. E.; Jones, K. S. A New Model for {311} Defects Based on *In-Situ* Measurements. *Int. Electron Devices Meet. Tech. Digest.* **2000**, 511-514.

6. Feenstra, R. M. Tunneling Spectroscopy of the (110) Surface of Direct-Gap III-V Semiconductors. *Phys. Rev. B* **1994**, 50, 4561-4570.

7. Hjort, M.; Wallentin, J.; Timm, R.; Zakharov, A. A.; Hakanson, U.; Andersen, J. N.; Lundgren, E.; Samuelson, L.; Borgstrom, M. T.; Mikkelsen, A. Surface Chemistry, Structure, and Electronic Properties from Microns to the Atomic Scale of Axially Doped Semiconductor Nanowires. *ACS Nano* **2012**, 6, 9679-9689.

8. Liu, H. J.; Owen, J. H. G.; Miki, K. Degenerate Electronic Structure of Reconstructed $MnSi_{1.7}$ Nanowires on Si (001). *J. Phys.: Condens. Matter* **2012**, 24, 095005.

9. Seiwatz, R.; Green, M. Space Charge Calculations for Semiconductors. *J. Appl. Phys.* **1958**, 29, 1034-1040.

10. Feenstra, R. M.; Stroscio, J. A. Tunneling Spectroscopy of the GaAs (110) Surface. *J. Vac. Sci. Technol. B* **1987**, 5, 923-929.

11. Lee, D. H.; Gupta, J. A. Tunable Field Control Over The Binding Energy of Single Dopants by a Charged Vacancy In GaAs. *Science* **2010**, 330, 1807-1810.

12. Feenstra, R. M. Electrostatic Potential for a Hyperbolic Probe Tip Near a Semiconductor. *J. Vac. Sci. Technol. B* **2003**, 21, 2080-2088.

13. Ishida, N.; Sueoka, K.; Feenstra, R. M. Influence of Surface States on Tunneling Spectra of n-type GaAs (110) surfaces. *Phys. Rev. B* **2009**, 80, 075320.

14. Feenstra, R. M.; Gaan, S.; Meyer, G.; Rieder, K. H. Low-Temperature Tunneling Spectroscopy of Ge(111)c(2X8) Surfaces. *Phys. Rev. B* **2005**, 71**,** 125316.

15. Feenstra, R. M.; Dong, Y.; Semtsiv, M. P.; Masselink, W. T. Influence of Tip-Induced Band Bending on Tunnelling Spectra of Semiconductor Surfaces. *Nanotechnology* **2007**, 18, 044015.

16. Dong, Y.; Feenstra, R. M.; Semtsiv, M. P.; Masselink, W. T. Band Offsets of InGaP/GaAs Heterojunctions by Scanning Tunneling Spectroscopy. *J. Appl. Phys.* **2008**, 103, 073704.

17. Gaan, S.; He, G. W.; Feenstra, R. M.; Walker, J.; Towe, E. Size, Shape, Composition, and Electronic Properties of InAs/GaAs quantum Dots by Scanning Tunneling Microscopy and Spectroscopy. *J. Appl. Phys.* **2010**, 108, 114315.

18. Pantzer, A.; Vakahy, A.; Eliyahu, Z.; Levi, G.; Horvitz, D.; Kohn, A. Dopant Mapping in Thin FIB Prepared Silicon Samples by Off-Axis Electron Holography. *Ultramicroscopy* **2014**, 138, 36-45.

19. Dunin-Borkowski, R. E.; Newcomb, S. B.; Kasama, T.; McCartney, M. R.; Weyland, M.; Midgley, P. A. Conventional and Back-Side Focused Ion Beam Milling for Off-Axis Electron Holography of Electrostatic Potentials in Transistors. *Ultramicroscopy* **2005**, 103, 67-81.

20. Houben, L.; Luysberg, M.; Brammer, T. Illumination Effects in Holographic Imaging of The Electrostatic Potential of Defects and pn Junctions in Transmission Electron Microscopy. *Phys. Rev. B* **2004**, 70, 165313.

21. Kohn, A.; Habibi, A. Adapting a JEM-2100F for Magnetic Imaging by Lorentz TEM. *JEOL News* **2012**, 47**,** 17-22.

22. McCartney, M. R.; Agarwal, N.; Chung, S.; Cullen, D. A.; Han, M. G.; He, K.; Li, L. Y.; Wang, H.; Zhou, L.; Smith, D. J. Quantitative Phase Imaging of Nanoscale Electrostatic and Magnetic Fields Using Off-Axis Electron Holography. *Ultramicroscopy* **2010**, 110, 375-382.